Characterisation of amorphous molybdenum silicide (MoSi) superconducting thin films and nanowires

OPEN ACCESS
IOP Publishing
Superconductor Science and Technology
Supercond. Sci. Technol. **30** (2017) 084010 (11pp)
https://doi.org/10.1088/1361-6668/aa76d8

Characterisation of amorphous molybdenum silicide (MoSi) superconducting thin films and nanowires

Archan Banerjee[1], Luke J Baker[1], Alastair Doye[2], Magnus Nord[2], Robert M Heath[1], Kleanthis Erotokritou[1], David Bosworth[3], Zoe H Barber[3], Ian MacLaren[2] and Robert H Hadfield[1]

[1] School of Engineering, University of Glasgow, Glasgow G12 8QQ, United Kingdom
[2] Scottish Universities Physics Alliance (SUPA) and School of Physics and Astronomy, University of Glasgow, Glasgow G12 8QQ, United Kingdom
[3] Department of Materials Science and Metallurgy, University of Cambridge, Cambridge CB3 0FS, United Kingdom

E-mail: a.banerjee.2@research.gla.ac.uk

Received 27 March 2017, revised 31 May 2017
Accepted for publication 2 June 2017
Published 12 July 2017

Abstract

We report on the optimisation of amorphous molybdenum silicide thin film growth for superconducting nanowire single-photon detector (SNSPD) applications. Molybdenum silicide was deposited via co-sputtering from Mo and Si targets in an Ar atmosphere. The superconducting transition temperature (T_c) and sheet resistance (R_s) were measured as a function of thickness and compared to several theoretical models for disordered superconducting films. Superconducting and optical properties of amorphous materials are very sensitive to short- (up to 1 nm) and medium-range order (~1–3 nm) in the atomic structure. Fluctuation electron microscopy studies showed that the films assumed an A15-like medium-range order. Electron energy loss spectroscopy indicates that the film stoichiometry was close to $Mo_{83}Si_{17}$, which is consistent with reports that many other A15 structures with the nominal formula A_3B show a significant non-stoichiometry with $A{:}B > 3{:}1$. Optical properties from ultraviolet (270 nm) to infrared (2200 nm) wavelengths were measured via spectroscopic ellipsometry for 5 nm thick MoSi films indicating high long wavelength absorption. We also measured the current density as a function of temperature for nanowires patterned from a 10 nm thick MoSi film. The current density at 3.6 K is 3.6×10^5 A cm^{-2} for the widest wire studied (2003 nm), falling to 2×10^5 A cm^{-2} for the narrowest (173 nm). This investigation confirms the excellent suitability of MoSi for SNSPD applications and gives fresh insight into the properties of the underlying materials.

Keywords: superconducting thin films, superconducting nanowire single-photon detector, amorphous superconductor, molybdenum silicide

(Some figures may appear in colour only in the online journal)

1. Introduction

Since the pioneering work of Buckel *et al* on the superconductivity of amorphous Bi deposited on a cryogenically cooled substrate [1], amorphous superconducting materials have been the subject of numerous experimental and theoretical research studies [2–4]. Initially, non-transition pure-metal-based amorphous superconductors were explored in

Table 1. Comparison of the superconducting properties of amorphous TM-based materials with those of the conventional SNSPD material NbN.

	NbN	MoSi	MoGe	WSi	NbSi
Bulk T_c (K)	16 [29]	7.5 [24]	7.4 [27]	5 [27]	3.1[30]
Thin film T_c (K) (Thickness (nm))	8.6 (3 nm) [29]	4.2 (4 nm) [24]	4.4 (7.5 nm) [27]	3.7 (4.5 nm) [27]	2 (10 nm) [31]
Band gap $2\Delta_0$ (meV)	4.9 [24]	2.28 [24]	2.2 [27]	1.52 [27]	0.94
Critical current density J_c (MA cm^{-2}) (measurement temperature (K))	2–4 (4.2 K) [29]	1.1–2.5 (1.7 K) [32]	1.2 (250 mK) [27]	0.8 (250 mK) [27]	0.14 (300 mK) [31]

detail [4, 5]. Though amorphous phase or structural disorder enhances the superconducting properties of such materials, they are structurally stable only at very low temperatures (<20 K). The superconducting properties of transition metals (TMs) and metal-based alloys have become an area of growing interest [6, 7]. Studies of TM-based amorphous alloy materials have shown that their superconducting properties are clearly affected by variations in their composition and amorphous character (e.g. through enhancement or suppression of the superconducting transition temperature); however, a clear advantage of TM alloys is the *stability* of the amorphous structure, even on cycling between room temperature and cryogenic temperatures. Potential applications in the field of superconducting detectors [8] or vortex memory devices [9] have motivated detailed investigations of TM-based amorphous superconductors. Several theoretical models have also been proposed to explain the subtle interplay between disorder and the superconducting to normal state transition, whilst correlating superconductivity to other material characteristics (e.g. sheet resistance and thickness) [10–12], which can be used to describe the physical properties of amorphous thin film systems. Optimisation of amorphous superconducting thin films for specific superconducting detector applications along with exploration of the relationship between superconductivity and various empirical material parameters remains an interesting problem.

Recently, several amorphous TM-based Type II superconducting materials (MoSi, MoGe and WSi) have been demonstrated to be highly promising alternative base materials for superconducting nanowire single-photon detector (SNSPD or SSPD) fabrication [13]. SNSPDs play a significant role as an enabling technology in advanced photon counting applications [14]. Emerging applications of these detectors include quantum key distribution [15], quantum computing [16], characterisation of quantum emitters [17], space-to-ground communications [18], integrated circuit testing [19] and single oxygen luminescence dosimetry for laser based cancer treatment [20]. Although polycrystalline NbN and NbTiN thin films have hitherto been the most widely used materials for SNSPD fabrication [21, 22], amorphous superconductors can offer various advantages [23]. They do not have strict substrate requirements and also have lower superconducting gap energies [24], giving a higher intrinsic single-photon detection efficiency at longer wavelengths. Although they have lower critical current density due to lower free carrier concentration, this also leads to a larger hotspot size during absorption of an incident photon [25].

A lower superconducting band gap ($2\Delta_0$) corresponds to a lower superconducting transition temperature (T_c), according to the Bardeen–Cooper–Schrieffer relation [26]:

$$2\Delta_0 = 3.53 k_B T_c. \quad (1)$$

Molybdenum silicide, with a composition of $Mo_{75}Si_{25}$, has a bulk T_c of ~7.5 K [27], which is comparatively high for a TM-based superconducting material. On the other hand, its bulk superconducting energy gap is ~2.28 meV [27] which is less than half of the energy gap of NbN (4.9 meV) [24]. As we can see from table 1, amorphous alloys such as WSi (the most commonly used amorphous thin film for high efficiency SNSPDs) or NbSi have very low bulk T_c. Hence, an expensive and complicated cooling system is required to run WSi based SNSPDs below 1 K in order to achieve high single-photon detection efficiency and low timing jitter. MoSi has a $T_c > 4$ K even in the thin film form, though its superconducting band gap is comparable to that of WSi. So, it could be an ideal base material for high performance SNSPDs which can be operated at a temperature >2 K using relatively cheap, less complex closed-cycle cryogenic systems [27]. Due to its low density of intrinsic pinning centres and larger Ginzburg–Landau parameter, MoSi is also an attractive material for flux-avalanche related applications [28].

SNSPDs fabricated from WSi amorphous thin films have demonstrated a system detection efficiency (SDE) of greater than 90% [8]. The first MoSi-based SNSPD was reported to achieve 18% efficiency at 1200 nm wavelength by Korneeva *et al* [33]. Verma *et al* have recently shown that by integrating detectors in an optical cavity, an enhanced efficiency of 87% at 1542 nm can be obtained with a 76 ps timing jitter [34, 35].

In this study, we have explored the growth and optimisation of amorphous MoSi thin films, in terms of the desirable superconducting properties for SNSPD fabrication. This work is built on a previous study of thick MoSi films [23]. Molybdenum silicide films were deposited using DC magnetron sputtering with argon plasma. Superconducting transition temperature was measured using a four-point measurement inside a closed-cycle Gifford–McMahon cryo-cooler (base temperature ~3 K) [36]. The variation of superconducting properties with sheet resistance and film thickness has been compared with several theoretical models. The material parameters extracted from these models concur with the amorphous and homogenously disordered nature of these films.

Recent studies have identified the important role played by microstructure and short or medium-range order in amorphous materials in determining their physical properties, including superconducting characteristics [37, 38]. Here, we report on a detailed investigation of the properties of amorphous MoSi. For the first time, fluctuation electron microscopy (FEM) has been used to investigate the local structural ordering of amorphous superconducting MoSi films. FEM shows that the films deposited in accordance with the optimised growth recipe (leading to the maximum T_c) assumes an A15-like structure over the range of a few atomic spacings, whilst there is no long-range crystallographic order. Electron energy loss spectroscopy (EELS) analysis was also performed, indicating the film stoichiometry was close to $Mo_{83}Si_{17}$. This differs slightly from the compositions reported by other groups: $Mo_{80}Si_{20}$ or $Mo_{75}Si_{25}$ [33, 34].

The complex refractive index of MoSi films has been measured using variable angle spectroscopic ellipsometry (VASE). This aids the simulation of optical absorption in SNSPDs. Critical current density is another important factor governing the performance of SNSPDs. We have measured the transport properties including the temperature dependence of critical current density in nanowires patterned from these MoSi thin films via electron beam lithography (EBL) and reactive ion etching (RIE).

2. Methods

In this section we introduce the principal experimental techniques used. Results are presented and discussed in the corresponding parts of section 3.

2.1. Thin film growth

Amorphous thin films can be created using various techniques e.g. sputtering [39, 40], particle irradiation [41], ion-mixing or ion-implantation [42], liquid quenching [43], atomic layer deposition [44] and electron-beam evaporation [45]. Amongst these methods, sputter deposition is the most useful fabrication technique for growing high quality superconducting thin films for nanoscale device applications. In this study, MoSi films were grown on various substrates in a load-locked ultrahigh vacuum (base pressure $<5 \times 10^{-9}$ Torr) sputter deposition system. Films were co-sputtered from Mo (99.99% purity, supplier: International Advanced Materials) and Si (99.999% purity, supplier: Kurt J Lesker Company Ltd) targets in an argon plasma environment. Both the targets had a diameter of 3 inches (i.e. a surface area of 45.54 cm^2).

The molybdenum target was sputtered using a DC power supply in constant current mode and the silicon target with an impedance matched radio frequency (RF) power supply. The distance between the targets and the substrate was 100 mm, mounted at an angle of 5° to the vertical in a confocal configuration. According to the specifications provided by the system manufacturer (Plassys Bestek, France (http://plassys.com)), combined with substrate rotation, at this distance the deposition is most uniform over a large area (maximum wafer diameter 150 mm). Except where specifically noted, all depositions were carried out with the substrate at room temperature. The substrate holder was rotated at a speed of 60 rotations per minute during deposition for better uniformity of the film growth. At the beginning of each deposition cycle, 30 sccm of argon was introduced in the process chamber keeping the throttle valve fixed at 80° (this sets total chamber pressure at 0.2 Pa). An approximate estimate of the composition of the films can be made from the deposition rate of each target. Film thickness has been measured by creating a step profile with the help of an ink pen before the film growth and measuring height of the step in atomic force microscopy. For a selection of samples, the measurement of film thickness has been cross checked in scanning transmission electron microscopy (STEM). Film growth was initially optimized on silicon substrates. Silicon has an advanced and mature fabrication technology and is an attractive substrate material for various SNSPD applications at telecommunication wavelength, including integrated quantum photonics [46] and self-aligned detectors [47].

Prior to each sample deposition, both targets were pre-sputtered for one minute to stabilise deposition conditions. At first, the discharge current of the Mo target was fixed at a specific value. Then, the RF power of Si target was varied keeping other conditions unchanged in order to tune the composition of MoSi films. In subsequent deposition runs, the same process was repeated for several fixed discharge current values for the Mo target, keeping other parameters unchanged. In the literature there are several definitions of T_c. We define it as the temperature at which resistance of the film (measured via a four-point current biased measurement) disappears or falls to zero in the R versus T curve.

2.2. Analysis of structure and composition

In order to better understand the atomic structure and composition of our MoSi films, we have employed a suite of advanced scanning transmission electron microscopy (STEM) techniques. A standard focussed ion beam (FIB) lift-out technique was used to prepare thinned samples for STEM analysis [48].

In order to study the amorphous structure in a thin film just a few nm thick, FEM was the only practical technique [49, 50]. This, in the Voyles and Muller formulation, requires the collection of large datasets of diffraction patterns from small sample volumes, typically collected using STEM with a probe size of the order of 1–2 nm.

EELS spectrum imaging (SI) was performed to analyse the composition of the films using a JEOL ARM200F transmission electron microscope operated at 200 kV equipped with a probe aberration corrector and a Gatan GIF Quantum ER spectrometer/energy filter. The probe convergence angle was 29 mrad and the spectrometer acceptance angle was 36 mrad, and all datasets were acquired in DualEELS mode, with an energy range for the high loss set to include the Si–K and Mo-$L_{2,3}$ edges.

2.3. Variable angle spectroscopic ellipsometry (VASE)

Accurate measurement of optical constants is crucial to the simulation of optical absorption in SNSPDs and is a key to integrating these devices with complex optical structures

(such as cavities, nanoantennas and waveguides). The complex refractive index of two of our MoSi films has been evaluated at room temperature using a J A Woollam and Co. VASE instrument. The spectral range of the VASE measurement was from 270 to 2200 nm wavelength.

2.4. Nanowire patterning of MoSi thin films

Along with the superconducting transition temperature, critical current (I_c) is another crucial parameter influencing the performance of superconducting devices. Typically, an optimal operation point for an SNSPD is set by the application of a bias current just below the critical current value of the specific device at the given operating temperature. Hence, a higher critical current density (J_c) is desirable for high sensitivity, low noise photon detection. We have surveyed the temperature dependence of the critical current density in a nanowire patterned from a MoSi thin film.

A 10 nm thick MoSi film has been patterned into nanowires of various design widths from 200 nm to 2 μm using a two-step EBL process. All EBL processes were carried out using a Vistec VB6 EBL tool at 100 keV. The first EBL step was used to define alignment markers and contact pads. After development, a 75 nm thick gold (with 15 nm Ti adhesion layer) layer was deposited by electron beam evaporation and lift-off. Nanowires were fabricated in the second EBL step. After that, nanowire patterns were transferred into the MoSi film by RIE using CF_4 gas.

3. Results and discussion

3.1. Analysis of superconducting properties of MoSi films

3.1.1. Growth and optimisation of MoSi. Figure 1(a) summarises the variation of T_c of 20 nm thick MoSi films deposited on silicon substrates as a function of Si target power, for several different Mo discharge currents. Deposition time was adjusted for each deposition cycle in such a way that the film thickness remains constant. Figure 1(b) shows the normalised resistance versus temperature curves for the 20 nm thick MoSi films deposited with 0.3 A discharge current applied at Mo target. Both the figures indicate that an optimal film composition has been achieved, with a T_c of 7.3 K (and a RRR of 0.95) for a 0.3 A Mo target discharge current and 125 W Si target RF power. For this optimised growth condition the film deposition rate was 0.138 nm s^{-1}, i.e. 2 min 45 s of deposition time was used to grow the 20 nm thick film.

3.1.2. Modelling of observed variation of transition temperature with film thickness. Ultrathin (<10 nm) superconducting films are required for SNSPD fabrication. Degradation of superconducting properties with a reduction in film thickness is a well known phenomenon, predicted by standard theories [51] and widely reported in literature. Once film thickness reaches a value comparable to the coherence length of the material, superconducting properties start to degrade sharply. Figure 2(a) shows how the properties of MoSi films change with film

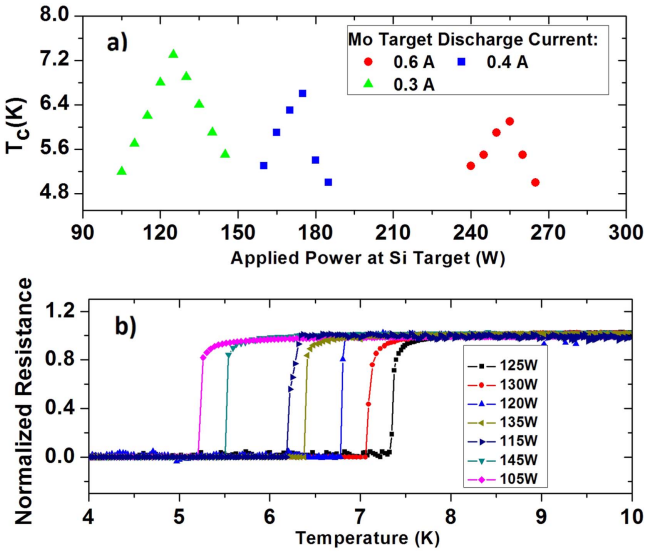

Figure 1. MoSi thin film growth optimisation: (a) T_c of 20 nm thick MoSi films deposited on silicon substrates as a function of power applied at the silicon target (optimum T_c has been achieved for a 0.3 A Mo target discharge current and 125 W Si target RF power; film compostion has been estimated through the deposition rate of the targets). (b) Normalised resistance versus temperature curve of 20 nm thick MoSi Films deposited with 0.3 A discharge current applied at the Mo target.

thickness. For a 5 nm thick film, we obtain a T_c of 5.5 K (RRR = 0.8). RRR increases with film thickness. Thinner films also have a greater sheet resistance as expected. Several theoretical models have been reported to explore the correlation between T_c, film thickness and sheet resistance and to explain the degradation of superconductivity with reduction in thickness. Finkel'stein modelled the T_c as a function of sheet resistance (R_s) for disordered superconducting materials (with no explicit dependence on thickness) [12]. According to this model:

$$\frac{T_c}{T_{co}} = \exp(\gamma)\left(\frac{1-X}{1+X}\right)^{1/\sqrt{2r}}, \tag{2}$$

where:

$$\gamma = \mathrm{Ln}(\hbar/\tau T_{co}k_B);\ X = \left(\frac{\sqrt{r/2}}{\frac{r}{4}+1/\gamma}\right) \tag{3}$$

and:

$$r = (e^2/2\pi^2\hbar)R_s. \tag{4}$$

Here T_{co} denotes the bulk superconducting transition temperature, $\hbar$ is the reduced Planck's constant, e is the elementary charge and γ is a fitting parameter. Figure 2(b) shows a plot of T_c versus R_s plot for our films. The fit with equation (2) was obtained by optimising T_{co} and γ. T_c data is fitted in the Finkel'stein model with T_{co} = 7.8 K and γ = 7.66 ± 0.1. Such a high value of the free fitting parameter γ would be consistent with the proposition that our films are strongly disordered. (For amorphous MoGe

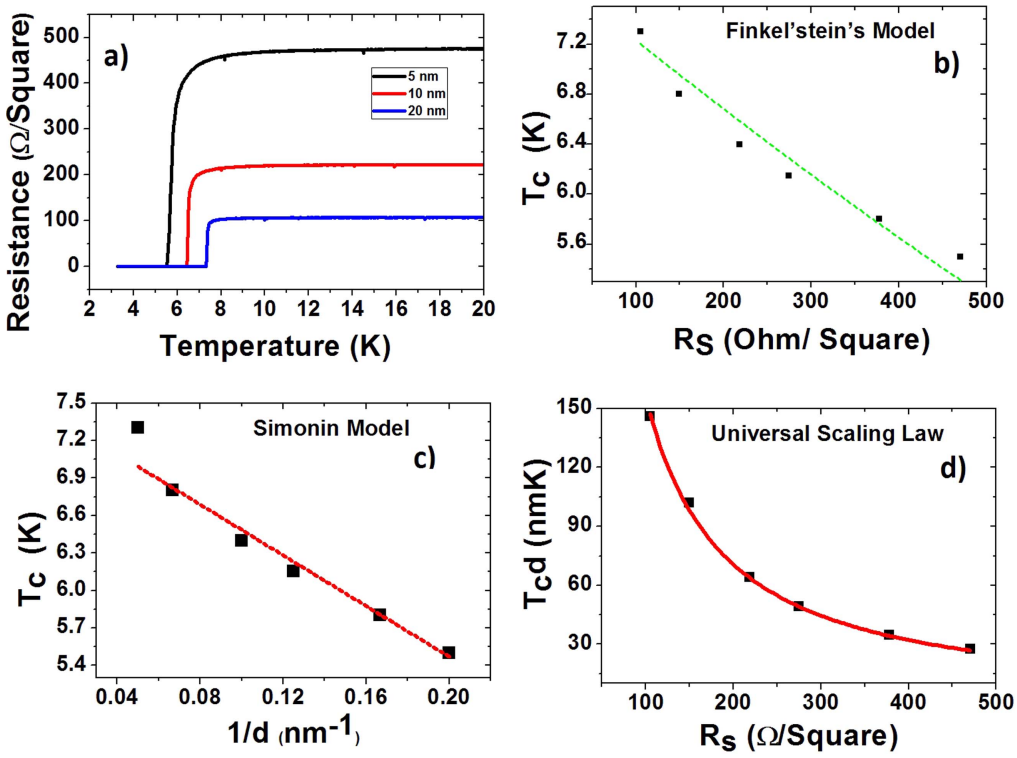

Figure 2. Variation of superconducting transition temperature with film thickness and comparison with theoretical models: (a) R versus T curve of MoSi film with three different thicknesses deposited at room temperature (Mo target discharge current: 0.3 A, Si target RF power: 125 W) (b) T_c versus R_s curve and its fit with Finkel'stein model ($\frac{T_c}{T_{co}} = \exp(\gamma)\left[\frac{1+X}{1-X}\right]^{1/\sqrt{2r}}$ [12]); $T_{co} = 7.8$ K and $\gamma = 7.66 \pm 0.1$ (c) Simonin model fit for T_c versus $1/d$ curve ($T_c = T_{co}(1-d_c/d)$ [11]); $T_{co} = 7.5 \pm 0.15$ K and $d_c = 1.46 \pm 0.15$ nm (d) T_cd versus R_s curve with its fit to the universal scaling law proposed by Ivry *et al* ($T_cd = AR_s^{-B}$ [10]); $A = 29436 \pm 487$ and $B = 1.14 \pm 0.03$.

Graybeal *et al* reported a value of 8.2 for the same parameter [52].) This suggests that the suppression of superconductivity due to fluctuation of Cooper pairs can be neglected because of the amorphous nature of the film.

From these values of T_{co} and γ we extract the mean scattering time $\tau = 4.61 \times 10^{-16}$ s for the 5 nm thick MoSi film, with a measured resistivity of 235.2 $\mu\Omega$ cm. Using this mean scattering time we can estimate an electron density $n = 3.24 \times 10^{22}/\text{cm}^3$, diffusion constant $D = 0.21 \times 10^{-4}\,\text{m}^2\,\text{s}^{-1}$ and a mean free path of 0.2 nm (assuming the free electron mass equals the rest mass of the electron). The free electron density is about 10 times lower than that reported in literature for NbN (for 6 nm thick NbN $1.26 \times 10^{23}/\text{cm}^3$ [53]) as expected for MoSi. The Ioffe–Regel parameter (k_fl) calculated based on a free electron model gives a value of 5.6 which is another indication of a homogeneously disordered film. However, our estimated value of k_fl is 2–3 times higher than the measured value of IR parameters which have been reported for strongly disordered films in the literature (2.6 for 5 nm thick TiN [54]). This higher value may be due to inaccuracy in the approximation of electron density from our data fit. Also, Graham *et al* have shown that for some amorphous materials, the metal-insulator transition may be observed at a much higher value (around $k_fl \sim 5.2$ for amorphous indium oxide [55]). Instead of $k_fl \sim 1$ they proposed $k_fl \sim \pi$ as the Ioffe–Regel criteria [55]. We also note (table 2) that both the free electron concentration and the Ioffe–Regel parameter show a gradual increase with film thickness.

Table 2. Free electron concentration n_e, Ioffe–Regel parameter (k_fl) and T_c of MoSi films with four different thicknesses d.

d (nm)	T_c (k)	n_e ($10^{22}/\text{cm}^3$)	k_fl
5	5.5	3.24	5.25
6	5.8	3.36	5.34
8	6.15	3.46	5.49
10	6.4	3.49	5.54

Although the comparison of T_c versus R_s data with the Finkel'stein model has given realistic values for various physical parameters of MoSi films, this model was actually initially proposed for two-dimensional films (where the film thickness is less than the mean free path of the electron). For films that have a thickness larger than their mean free path (which is the case here), it includes a correction factor in the expression for mean scattering time $\tau^* = (d/l)^2\tau$; for film thickness $d = 5$ nm, assuming a mean free path $l = \sim 0.2$ nm, we find that $\tau = 0.1844 \times 10^{-16}$ s and $D = 0.0084 \times 10^{-4}\,\text{m}^2\,\text{s}^{-1}$. This value of the diffusion coefficient is much smaller than the value reported in literature [56]. Thus, we did not take into consideration the correction factor here. The extraction of selected physical parameters from alternative measurements and

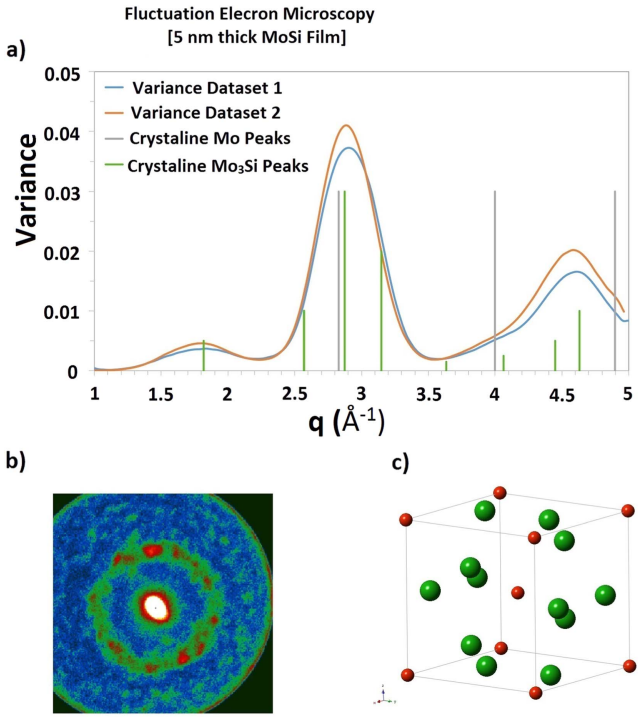

Figure 3. Fluctuation electron microscopy (FEM) of 5 nm thick MoSi film: (a) Variance plot of diffracted intensity; (b) diffraction pattern obtained from one pixel in the MoSi film; (c) model of A15 crystal structure: in the cubic unit cell 2 Si atoms (Red) occupy (0, 0, 0) and (1/2, 1/2, 1/2) positions whereas 6 Mo atoms (Green) are situated at (1/4, 0, 1/2); (1/2, 1/4, 0); (0, 1/2, 1/4); (3/4, 0, 1/2); (1/2, 3/4, 0); and (0, 1/2, 1/4) positions.

comparing them with our results may be helpful for more accurate modelling.

Simonin [11] derived a simple model based on Ginzburg–Landau theory describing the correlation between T_c and film thickness resulting in

$$T_c = T_{co}(1 - d_c/d). \quad (5)$$

The fitting parameter d_c is called the critical thickness. Figure 2(c) shows a plot of T_c versus $1/d$ and shows how equation (5) is fitted with the data. The data point related to the 20 nm thick film (thickest of the set) deviates from the fit, but the rest of the data fit well with a least squares fit using a $T_{co} = 7.5 \pm 0.15$ K and $d_c = 1.46 \pm 0.15$ nm (theoretically, this is the thickness below which the superconducting properties of the films will disappear). These values are in good agreement with literature [57]. Critical thickness can be related to the BCS interactional potential V by $d_c = 2a/N(0)V$ where $N(0)$ is the density of states at Fermi level and a is the Thomas–Fermi screening length. From Osofsky *et al* [57], we obtain $N(0)V = 0.086$ and $a \sim 0.06$ nm for MoSi. Hence, $d_c \sim 1.4$ nm.

Ivry *et al* [10] proposed an empirical universal scaling law which takes into account the effects of both d and R_s on T_c. According to this law, film thickness, sheet resistance and transition temperature scale as $T_c d(R_s)$ and leads to the following power law:

$$T_c d = AR_s^{-B}. \quad (6)$$

Figure 2(d) depicts how the universal scaling law fits to the MoSi growth data. Values of the fitting parameters are $A = 29436 \pm 487$ and $B = 1.14 \pm 0.03$ As discussed by Ivry *et al* [10], for amorphous films B is greater than one.

One can see a clear and accurate trend when we plot $T_c d$ as a function of R_s (figure 2(d)). For amorphous films, dependence on sheet resistance dominates over the thickness dependence. This is why the data point corresponding to the thickest film deviates from the Simonin model fit [11]. At the same time, the Finkel'stein model [12] fits more quantatively with all the data points (figure 2(b)). The universal scaling law takes into consideration both the effects of sheet resistance and thickness. Hence, it provides a far more accurate fit for our MoSi data. A higher value of the fitting parameter B also suggests that the film is amorphous which dominates the sheet resistance dependence.

3.2. Analysis of atomic structure and composition using STEM

It can be seen from the previous reports that a slight modification of the optimised deposition conditions (e.g. substrate cooling or HF treatment of substrates) measurably affects the superconducting properties of MoSi films in various ways [23]. Such variations in the deposition environment influence the short range structural ordering of an amorphous film. Bieger *et al* [58] concluded that the superconducting properties of amorphous materials are sensitive to short range order, based on resistivity measurements. In the crystalline state, Mo_3Si with an A15 structure has a very low bulk T_c ($\sim$1.3 K) [59]. Lattice disorder promotes its superconducting properties to a large extent [60, 61]. The effect of material properties on superconducting transition temperature can be described by McMillan's Parameter (given by $\lambda = \frac{N(0)\langle J^2\rangle}{M\langle w^2\rangle}$; where $N(0)$ is the density of states at the Fermi level, $\langle w^2\rangle$ denotes average phonon frequency, M is ion mass and $\langle J^2\rangle$ is the average electron–phonon coupling matrix) [62]. Lattice disorder increases T_c due to an enhancement in $N(0)$ and weakening of the phonon mode. The electron–phonon coupling matrix $\langle J^2\rangle$ is a function of the structure factor. Hence, any modification in short range structural order or 'amorphous nature' will influence McMillan's parameter and the superconducting properties. It is, consequently, crucial to investigate the local structural ordering of amorphous MoSi films, although preferably with more direct methods.

Diffraction patterns were collected from the MoSi thin film sample for the purpose of FEM analysis using a Medipix-3 active pixel detector attached to our JEOL ARM200F at the 35 mm camera port [63]. The illumination of the microscope was adjusted by turning the objective lens off and working in aberration-corrected Lorentz mode [64] to produce small probe convergence angles to increase resolution in reciprocal space. In the scans recorded, several thousand diffraction patterns were acquired from the layer at about 1 nm step size, as well as diffraction patterns from the areas above (gold) and

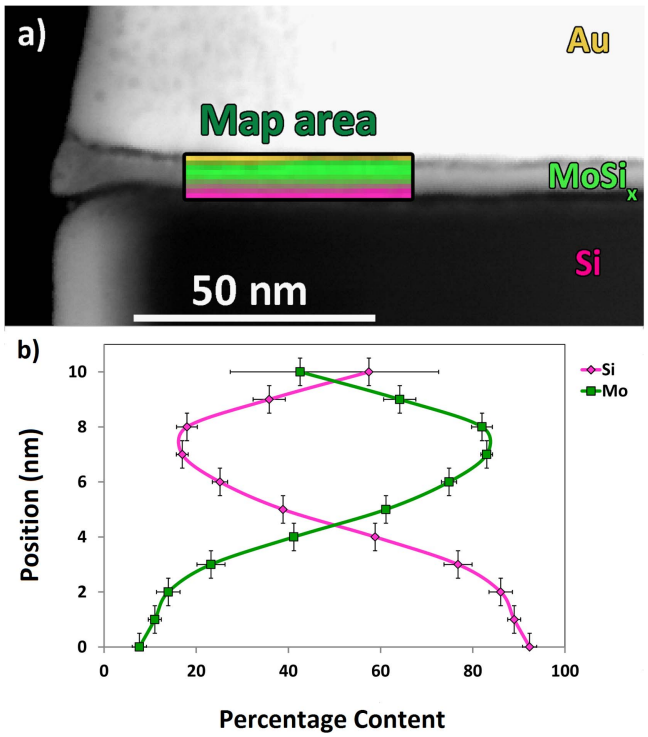

Figure 4. Investigating the composition of uncapped co-sputtered MoSi films via electron energy loss spectroscopy (EELS): (a) dark field image of the focussed ion beam (FIB) cross section of MoSi film, with the scan area indicated by the black box (coloured elemental map shows the silicon substrate, MoSi film and gold layer deposited on top of the film. The Si substrate in the lower part of the figure; the MoSi film is a horizontal band through the middle and the gold layer on the top added to protect the film during FIB sectioning). (b) Averaged elemental percentage composition from bottom to top (from the substrate across the film). An error bar has been added across the position axis to indicate the resolution or step size of the scan (1 nm).

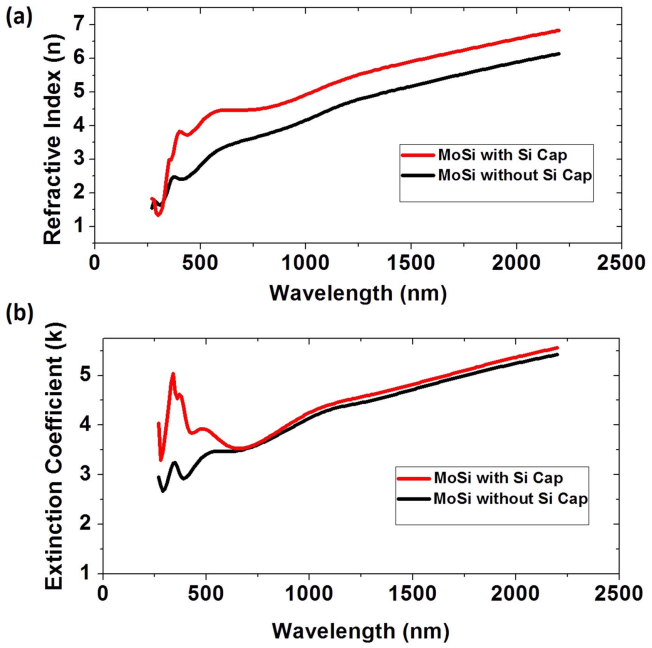

Figure 5. Complex refractive index measurement for 5 nm thick MoSi films using variable angle spectroscopic ellipsometry (VASE). (a) Refractive index measurement of MoSi film with a Si cap and MoSi film without a Si cap; (b) extinction coefficient measurement of MoSi film with a Si cap and MoSi film without a Si cap.

below (silicon), which were used for calibration of the diffraction patterns. A typical diffraction pattern recorded from the 5 nm thick MoSi film is shown in the figure 3(b). The variance of all patterns from the central portion of the layer was calculated as a function of q ($=2\pi k = 4\pi\sin\theta/\lambda$) using the method of Hart *et al* [65]. A small broad peak in the variance occurs at a q value of around 1.8 Å^{-1}, while larger peaks are visible around ~2.85 Å^{-1} and ~4.6 Å^{-1}. Superimposing the locations of diffraction peaks for both polycrystalline body-centered cubic (bcc) Mo and A15 structured Mo_3Si, the observed variance plots (figure 3(a)) have broad peaks where crystalline Mo_3Si would have sharp peaks and do not match well to metallic Mo.

Figure 4 shows a high angle annular dark field STEM image of a FIB cross section of the layer structure: some gold is evaporated onto the top of the film to protect it from Ga ion-implantation damage during FIB preparation. The datasets obtained from the EELS SI were quantified using the *Elemental Quantification* plugin for Digital Micrograph, which is a model-based EELS fitting routine, which includes explicit account for multiple scattering when working with DualEELS datasets. The cross sections for EELS quantification were the Hartree-Slater cross sections provided by Gatan.

The results of the quantification are shown in figure 4 as a graph of Mo and Si percentages in a line trace from the substrate into the film. It is clearly seen that the Mo content in the film peaks at the centre at about 83%, before a little excess Si is found at the surface.

This composition of 83% Mo and 17% Si is slightly different from the composition of the MoSi thin films usually reported in the literature for superconducting detector fabrication. However, in a previous study Bosworth *et al* [23] reported $Mo_{83}Si_{17}$ as the optimised composition for amorphous MoSi thin films in terms of superconducting properties. They showed that T_c for a 100 nm thick MoSi film decreases sharply if Si content in the film stoichiometry exceeds 17%. Zhao *et al* [66] demonstrated that a 1 μm thick MoSi film deposited on a liquid nitrogen cooled substrate achieve a maximum T_c when the Si content is around 15.8%. So, the 'Mo-rich' composition of the thin films we have optimised has already been mentioned in previous reports. Optimum composition of the film can also be influenced by configuration of the deposition systems. Overall, the STEM analysis has shown the existence of an A15-like atomic structure over a short or medium atomic range (less than 2 nm, corresponding to the probe size) and a slightly 'Mo-rich' off-stoichiometric composition (83:17 instead of the stoichiometric 75:25) in the MoSi films.

3.3. Measurement of optical constants for MoSi from UV to infrared wavelengths

Figure 5 presents the measurement of optical constants of amorphous MoSi films. All the films were grown at room temperature. We used plasma-enhanced chemical vapour

deposition to deposit a 390 nm thick layer of SiO_2 on several silicon substrates. For the first sample, we sputtered a 5 nm thick MoSi film on top of this substrate. For the second, we grew a 5 nm thick MoSi film with a protective Si capping layer (~4 nm thick) on top. Both the films have been deposited following the optimised recipe described in section 3.1 (these films have a T_c of 5.3 K with a RRR 0.83). As reported elsewhere [32], during the SNSPD device fabrication process, environmental contact may affect the superconducting properties of the films by surface oxidation. The presence of the capping layer may help to prevent possible degradation of the film during fabrication and atmospheric exposure. It should be noted that the silicon capping layer does not influence the superconducting properties of the MoSi film (we have verified this by low temperature testing). However the optical properties may be changed due to the presence of the capping layer.

The SiO_2 layer underneath the MoSi film acts as a transparent layer below the absorbing films and helped to break parameter correlation between optical constants and film thickness by interference enhancement during VASE measurement. The ellipsometric data was modelled with several Lorentz oscillators. From the figure 5, it is clear that MoSi films have a high extinction coefficient (k), leading to high optical absorption across the infrared range. The presence of the Si capping layer slightly enhances the extinction coefficient. The enhancement in absorption coefficient due to the Si capping layer is more pronounced for $\lambda < 600$ nm. This wavelength range is well above the gap energy of Si, so the Si is acting as an additional absorbing layer. Over the IR range a slight enhancement in k for the Si capping is still noticeable. Hence, the use of thin MoSi films in superconducting detectors will lead to higher optical efficiency of the devices. We can also see that the $k(\lambda)$ curve of MoSi shows a continuous sharp increase even in the higher wavelength region (1500–2200 nm). Hence, MoSi can serve as an optically efficient material for mid-infrared SNSPD detectors.

3.4. Transport properties of patterned superconducting MoSi nanowires

The superconducting properties of MoSi nanowires were investigated in a closed-cycle cryostat based on a two stage pulsed tube cooler. The base operating temperature of the cryostat is 3.5 K.

I–V curves for the device were recorded using a four-point measurement setup. A Keithley 238 current source was used to bias the device. The device is connected to the measurement circuit using SMA coaxial cables. While recording current-voltage characteristics, the compressor of the cryostat was turned on and off, allowing the cryostat temperature to vary between 3.5 and 6.5 K (monitored closely with a silicon diode thermometer). The cryostat took 2 min and 35 s to warm up from its base temperature to 6.5 K. At a given temperature, critical current increases with wire width as expected. Critical current density was calculated using the cross sectional area of each nanowire. Figure 6 depicts the variation of critical current density with measurement

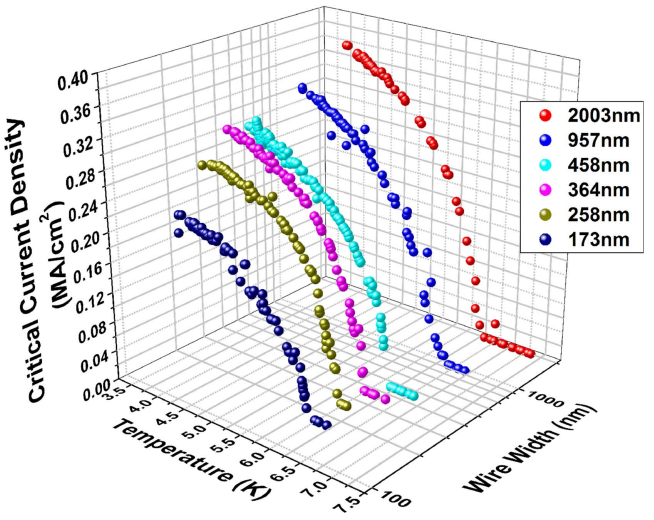

Figure 6. Transport measurement of nanowires patterned in a 10 nm thick MoSi thin film: critical current density versus temperature curve of nanowires having different widths (widths of the nanowires have been corrected from SEM inspection).

temperature for different wire widths. Scanning electron microscopy (SEM) was used to measure the accurate wire width after fabrication. The 2003 nm wide wire showed a critical current density of 0.36 MA cm^{-2} at 3.6 K. For a Type II superconductor, dependence of critical current on temperature in the dirty limit can be described by the relations [67, 68]

$$I_c(T) = I_c(0)\frac{\Delta(T)}{\Delta(0)}\tanh\left[\frac{\Delta(T)}{2k_BT}\right] \tag{7}$$

and

$$\Delta(T) = \Delta(0)\tanh\left[1.82\left[1.018\left(\frac{T_c}{T}-1\right)\right]^{0.51}\right], \tag{8}$$

where I_c(T) and $\Delta(T)$ denotes the measured critical current and superconducting energy gap at the specific measurement temperature and $\Delta(0)$ is the energy gap at absolute zero. We fitted critical current versus temperature data from MoSi nanowires to the above equations using $I_c(0)$, T_c and $2\Delta(0)$ as the fitting parameters. Figures 7(a) and (b) demonstrate how T_c and the values of superconducting band gap obtained from the curve fitting vary over the nanowire width.

It is evident that all the nanowires (2003–173 nm width) show a similar trend of superconducting transport properties. T_c is slightly depressed with decreasing wire width (from 6.23 to 5.94 K). Though critical current decreases consistently with wire width (as expected) all the nanowires show a common trend of variation in critical current density with temperature (figure 6). Also, at any specific measurement temperature there is a slow reduction in critical current density values with decreasing wire width. The nanowire of 2003 nm width shows a critical current density of 0.36 MA cm^{-2} measured at 3.6 K. The thinnest nanowire (173 nm wide) shows a comparatively lower J_c of 0.2 MA cm^{-2}. This deviation along

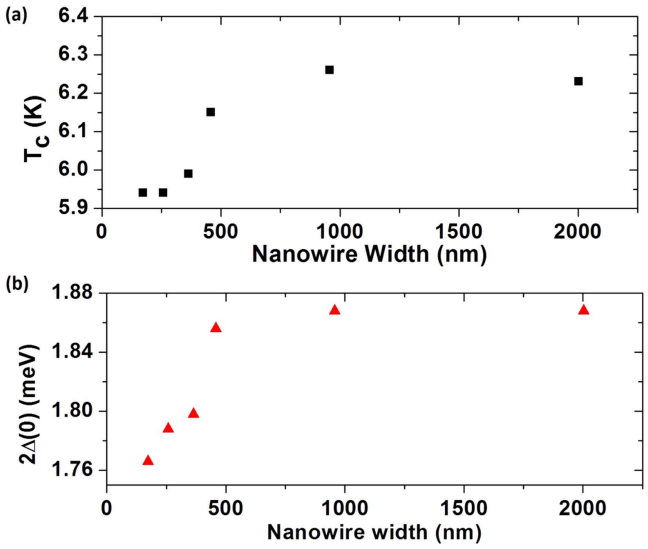

Figure 7. (a) and (b) Variation of transition temperature (T_c) and superconducting energy gap $2\Delta(0)$ with nanowire width. (Transition temperature has been measured by low temperature testing and $2\Delta(0)$ has been extracted from the fitting of critical current versus temperature data with equations (7) and (8).)

with the fluctuation in values of J_c in the rest of the nanowires can be explained by inhomogeneity caused during the nanowire fabrication. Close SEM inspection indicates the edges of the nanowires may be damaged with redeposition of etch debris and e-beam resist which would lead to a reduction in the superconducting cross-section. This effect would be strongest (proportionately to the width) in the narrowest wires. The superconducting band gaps of the nanowires based on our thin films are much smaller than the bulk energy gap of MoSi (~2.26 meV) reported in literature [27]. For wire width >458 nm $2\Delta(0)$ assumes a value ~1.87 meV; for the 173 nm wide nanowire it drops to 1.77 meV.

Lita *et al* [27] reported a critical current density of ~1.3 MA cm^{-2} at 250 mK for a 1 μm wide nanowire patterned on a 6.3 nm thick MoSi film. Korneeva *et al* [32] have showed critical current density varies from 1.1 to 2.5 MA cm^{-2} for nanowire patterned meander devices on 4 nm thick MoSi films measured at 1.7 K. Although we report lower critical current density values here, we are measuring in a significantly higher temperature range (3.6 K and above).

To date we have reported a low temperature photoresponse map recorded at 350 mK (corresponding to a maximum SDE, inclusive of optical coupling losses, of approximately 5% at 1550 nm wavelength under the perpendicular illumination condition) from a waveguide integrated SNSPD fabricated on a 10 nm thick MoSi thin film deposited at the University of Cambridge with a similar composition ($Mo_{83}Si_{17}$) [69]. At present we are exploring the optical response of full SNSPD devices fabricated based on the MoSi films we have optimised in this study.

4. Conclusion

We have carried out a comprehensive study of the superconducting, structural and optical properties of co-sputtered amorphous molybdenum silicide thin films. We have optimised MoSi film growth and demonstrated a T_c of 5.5 K for a 5 nm thick film. By comparing our transition temperature measurement data with several theoretical models (Finkel'stein, Simonin and Ivry) we find that the room temperature sheet resistance is strongly linked to the resulting T_c of the amorphous films. We have employed advanced STEM techniques including FEM to reveal that the film consists of short range nano crystalline structure which is similar to an A15 Mo_3Si structure. Based on the sputter deposition rates, the composition of the film is closer to 83:17 than 75:25. This is typical of A15 structures and could be due to either a significant vacancy population on the corner of *B* (Si) sites of A_3B (Mo_3Si) structure, or alternatively substitution of *A* (Mo) atoms on some of the *B* (Si) sites [70]. We note that amongst the groups studying amorphous superconductors for SNSPDs, some report success with co-sputtered films [35], whereas others have chosen sputtering from a single alloy target [34]. It would be of considerable interest to apply the FEM technique in order to compare co-sputtered material with alloy target sputtered material, and to identify how best to achieve precise control of amorphous texture. VASE studies have also been carried out to determine the complex refractive index of uncapped and Si capped MoSi films. This data is important for integrating MoSi SNSPD into advanced optical structures such as waveguides and cavities and tailoring devices for specific wavelengths in future. Finally, transport properties including critical current and its dependence on temperature have been evaluated after nanowire patterning (in range of 2003 nm width down to 173 nm width) in a 10 nm thick film. The current density measured at 3.6 K (in the range 0.36 to 0.2 MA cm^{-2}, diminishing with wire width) indicates nanowires are suitable for SNSPD operation at elevated temperature. This work has important implications in the optimisation of MoSi films for next generation SNSPDs, for realisation of uniform large area SNSPD focal plane arrays and for integration with advanced optical architectures such as quantum photonic waveguide circuits.

Acknowledgments

AB and RHH thank the staff of the James Watt Nanofabrication Centre (JWNC) at the University of Glasgow for support. The authors acknowledge the late Dr Patrick Smutek of Plassys Bestek France for expert support in the design and delivery of the UHV sputter deposition tool. RHH and ZHB acknowledge support from the Engineering and Physical Sciences Research Council (EPSRC) through grants EP/I036273/1, EP/L024020/1, EP/M01326X/1 and EP/I036303/1. AD was supported by the EPSRC CDT in Integrative Sensing and Measurement, Grant Number EP/L016753/1. RHH acknowledges a European Research Council consolidator grant (IRIS 648604).

References

[1] Buckel W 1954 Elektronenbeugungs-aufnahmen von dünnen metallschichten bei tiefen temperaturen *Z. Phys.* **138** 136–50

[2] Tsuei C C 1981 Amorphous superconductors *Superconductor Materials Science: Metallurgy, Fabrication, and Applications* ed S Foner and B B Schwartz (Boston, MA: Springer US) pp 735–56

[3] Johnson W L and Poon S J 1975 Superconductivity in amorphous and microcrystalline transition−metal alloys *J. Appl. Phys.* **46** 1787

[4] Bergmann G 1976 Amorphous metals and their superconductivity *Phys. Rep.* **27** 159–85

[5] Havinga E E 1968 Bandstructure and superconductivity of non-transition metals *Phys. Lett.* A **26** 244–6

[6] Collver M M and Hammond R H 1973 Superconductivity in 'amorphous' transition-metal alloy films *Phys. Rev. Lett.* **30** 92–5

[7] Watson P, Bandyopadhyay B, Bo Y, Rathnayaka D and Naugle D G 1988 Superconductivity in 3d series amorphous transition metal alloys *Mater. Sci. Eng.* **99** 175–8

[8] Marsili F *et al* 2013 Detecting single infrared photons with 93% system efficiency *Nat. Photon.* **7** 210–4

[9] Miyahara K, Mukaida M, Tokumitsu M, Kubo S and Hohkawa K 1987 Abrikosov vortex memory with improved sensitivity and reduced write current levels *IEEE Trans. Magn.* **23** 875–8

[10] Ivry Y, Kim C S, Dane A E, De Fazio D, McCaughan A N, Sunter K A, Zhao Q and Berggren K K 2014 Universal scaling of the critical temperature for thin films near the superconducting-to-insulating transition *Phys. Rev.* B **90** 214515

[11] Simonin J 1986 Surface term in the superconductive Ginzburg–Landau free energy: application to thin films *Phys. Rev.* B **33** 7830–2

[12] Finkel'stein A M 1994 Suppression of superconductivity in homogeneously disordered systems *Physica* B **197** 636–48

[13] Natarajan C M, Tanner M G and Hadfield R H 2012 Superconducting nanowire single-photon detectors: physics and applications *Supercond. Sci. Technol.* **25** 63001

[14] Hadfield R H 2009 Single-photon detectors for optical quantum information applications *Nat. Photon.* **3** 696–705

[15] Collins R J, Hadfield R H, Fernandez V, Nam S W and Buller G S 2007 Low timing jitter detector for gigahertz quantum key distribution *Electron. Lett.* **43** 180

[16] Chen J, Altepeter J, Medic M, Lee K, Gokden B, Hadfield R, Nam S and Kumar P 2008 Demonstration of a quantum controlled-NOT gate in the telecommunications band *Phys. Rev. Lett.* **100** 133603

[17] Hadfield R H, Stevens M J, Mirin R P and Nam S W 2007 Single-photon source characterization with twin infrared-sensitive superconducting single-photon detectors *J. Appl. Phys.* **101** 103104

[18] Grein M E *et al* 2011 Design of a ground-based optical receiver for the lunar laser communications demonstration *2011 Int. Conf. Sp. Opt. Syst. Appl. (ICSOS),* pp 78–82

[19] Zhang J *et al* 2003 Noninvasive CMOS circuit testing with NbN superconducting single-photon detectors *Electron. Lett.* **39** 1086

[20] Gemmell N R, McCarthy A, Liu B, Tanner M G, Dorenbos S D, Zwiller V, Patterson M S, Buller G S, Wilson B C and Hadfield R H 2013 Singlet oxygen luminescence detection with a fiber-coupled superconducting nanowire single-photon detector *Opt. Express* **21** 5005

[21] Marsili F, Gaggero A, Li L H, Surrente A, Leoni R, Lévy F and Fiore A 2009 High quality superconducting NbN thin films on GaAs *Supercond. Sci. Technol.* **22** 95013

[22] Shiino T, Shiba S, Sakai N, Yamakura T, Jiang L, Uzawa Y, Maezawa H and Yamamoto S 2010 Improvement of the critical temperature of superconducting NbTiN and NbN thin films using the AlN buffer layer *Supercond. Sci. Technol.* **23** 45004

[23] Bosworth D, Sahonta S-L, Hadfield R H and Barber Z H 2015 Amorphous molybdenum silicon superconducting thin films *AIP Adv.* **5** 87106

[24] Verma V B, Lita A E, Vissers M R, Marsili F, Pappas D P, Mirin R P and Nam S W 2014 Superconducting nanowire single photon detectors fabricated from an amorphous $Mo_{0.75}Ge_{0.25}$ thin film *Appl. Phys. Lett.* **105** 0–5

[25] Baek B, Lita A E, Verma V and Nam S W 2011 Superconducting a-W_xSi_{1-x} nanowire single-photon detector with saturated internal quantum efficiency from visible to 1850 nm *Appl. Phys. Lett.* **98** 251105

[26] Tinkham M 2004 *Introduction to Superconductivity* (*Dover Books on Physics*) vol 1 (New York: Dover)

[27] Lita A E, Verma V B, Horansky R D, Shainline J M, Mirin R P and Nam S 2015 Materials development for high efficiency superconducting nanowire single-photon detectors *MRS Proc.* **1807** 1–6

[28] Kubo S 1988 Superconducting properties of amorphous MoX (X = Si, Ge) alloy films for Abrikosov vortex memory *J. Appl. Phys.* **63** 2033

[29] Marsili F, Bitauld D, Fiore A, Gaggero A, Mattioli F, Leoni R, Benkahoul M and Lévy F 2008 High efficiency NbN nanowire superconducting single photon detectors fabricated on MgO substrates from a low temperature process *Opt. Express* **16** 3191

[30] Proslier T, Klug J A, Elam J W, Claus H, Becker N G and Pellin M J 2011 Atomic layer deposition and superconducting properties of NbSi films *J. Phys. Chem.* C **115** 9477–85

[31] Dorenbos S N, Forn-Díaz P, Fuse T, Verbruggen A H, Zijlstra T, Klapwijk T M and Zwiller V 2011 Low gap superconducting single photon detectors for infrared sensitivity *Appl. Phys. Lett.* **98** 251102

[32] Korneeva Y P *et al* 2013 Superconducting single-photon detector made of MoSi film arXiv:1309.7074v1

[33] Korneeva Y P *et al* 2014 Superconducting single-photon detector made of MoSi film *Supercond. Sci. Technol.* **27** 95012

[34] Verma V B *et al* 2015 High-efficiency superconducting nanowire single-photon detectors fabricated from MoSi thin-films *Opt. Express* **23** 33792

[35] Caloz M, Korzh B, Timoney N, Weiss M, Gariglio S, Warburton R J, Schönenberger C, Renema J, Zbinden H and Bussières F 2017 Optically probing the detection mechanism in a molybdenum silicide superconducting nanowire single-photon detector *Appl. Phys. Lett.* **110** 083106

[36] Erotokritou K 2014 *Low temperature characterization of superconducting thin films and devices* UK: University of Glasgow private communication

[37] Buschow K H J 1984 Short-range order and thermal stability in amorphous alloys *J. Phys. F: Met. Phys.* **14** 593–607

[38] Lefebvre J, Hilke M and Altounian Z 2009 Superconductivity and short-range order in metallic glasses $Fe_xNi_{1-x}Zr_2$ *Phys. Rev.* B **79** 184525

[39] Raible M, Mayr S G, Linz S J, Moske M, Hänggi P and Samwer K 2000 Amorphous thin-film growth: theory compared with experiment *Europhys. Lett.* **50** 61–7

[40] Moustakas T D 1982 Studies of thin-film growth of sputtered hydrogenated amorphous silicon *Sol. Energy Mater.* **8** 187–204

[41] Sweedler A R, Schweitzer D G and Webb G W 1974 Atomic ordering and superconductivity in high-T_c A-15 compounds *Phys. Rev. Lett.* **33** 168–72

[42] Tsaur B Y, Liau Z L and Mayer J W 1979 Ion-beam-induced silicide formation *Appl. Phys. Lett.* **34** 168
[43] Duwez P 1976 Structure and properties of glassy metals *Annu. Rev. Mater. Sci.* **6** 83–117
[44] Nilsen O, Karlsen O B, Kjekshus A and Fjellvåg H 2007 Simulation of growth dynamics in atomic layer deposition: I. Amorphous films *Thin Solid Films* **515** 4527–37
[45] Sontheimer T *et al* 2010 Challenges and opportunities of electron beam evaporation in the preparation of poly-Si thin film solar cells *2010 35th IEEE Photovoltaic Specialists Conf.* (Piscataway, NJ: IEEE) pp 000614–9
[46] Pernice W H P, Schuck C, Minaeva O, Li M, Goltsman G N, Sergienko A V and Tang H X 2012 High-speed and high-efficiency travelling wave single-photon detectors embedded in nanophotonic circuits *Nat. Commun.* **3** 1325
[47] Miller A J, Lita A E, Calkins B, Vayshenker I, Gruber S M and Nam S W 2011 Compact cryogenic self-aligning fiber-to-detector coupling with losses below one percent *Opt. Express* **19** 9102
[48] Giannuzzi L A and Stevie F A 1999 A review of focused ion beam milling techniques for TEM specimen preparation *Micron* **30** 197–204
[49] Treacy M M J and Gibson J M 1996 Variable coherence microscopy: a rich source of structural information from disordered materials *Acta Crystallogr.* A **52** 212–20
[50] Voyles P M and Muller D A 2002 Fluctuation microscopy in the STEM *Ultramicroscopy* **93** 147–59
[51] Usadel K D 1970 Generalized diffusion equation for superconducting alloys *Phys. Rev. Lett.* **25** 507–9
[52] Graybeal J M and Beasley M R 1984 Localization and interaction effects in ultrathin amorphous superconducting films *Phys. Rev.* B **29** 4167–9
[53] Semenov A *et al* 2009 Optical and transport properties of ultrathin NbN films and nanostructures *Phys. Rev.* B **80** 54510
[54] Hadacek N, Sanquer M and Villé J-C 2004 Double reentrant superconductor-insulator transition in thin TiN films *Phys. Rev.* B **69** 24505
[55] Graham M R, Adkins C J, Behar H and Rosenbaum R 1998 Experimental study of the Ioffe–Regel criterion for amorphous indium oxide films *J. Phys. Condens. Matter* **10** 809–19
[56] Zhang X, Engel A, Wang Q, Schilling A, Semenov A, Sidorova M, Hübers H-W, Charaev I, Ilin K and Siegel M 2016 Characteristics of superconducting tungsten silicide W_x Si_{1-x} for single photon detection *Phys. Rev.* B **94** 174509
[57] Osofsky M S, Soulen R J, Claassen J H, Trotter G, Kim H and Horwitz J S 2001 New insight into enhanced superconductivity in metals near the metal-insulator transition *Phys. Rev. Lett.* **87** 197004
[58] Bieger J, Adrian H, Müller P, Saemann-Ischenko G and Haase E L 1980 Superconductivity and electrical resistivity of amorphous $Nb_{75}Ge_{25}$ and $Nb_{80}Si_{20}$ after heavy ion irradiation at low temperature *Solid State Commun.* **36** 979–82
[59] Tütüncü H M, Bağcı S and Srivastava G P 2010 Electronic structure, phonons, and electron–phonon interaction in Mo_3Si *Phys. Rev.* B **82** 214510
[60] Lehmann M, Saemann-Ischenko G, Adrian H and Nölscher C 1981 Disordered A15 compounds from the Matthias-Valley: Mo_3Ge and Mo_3Si *Physica* B+C **107** 473–4
[61] Kar'kin A E, Voronin V I, D'yachkova T V, Kadyrova N I, Tyutyunik A P, Zubkov V G, Zainulin Y G, Sadovskii M V and Goshchitskii B N 2001 Superconducting properties of the atomically disordered MgB_2 compound *J. Exp. Theor. Phys. Lett.* **73** 570–2
[62] McMillan W L 1968 Transition temperature of strong-coupled superconductors *Phys. Rev.* **167** 331–44
[63] Mir J A *et al* 2016 Medipix3-demonstration and understanding of near ideal detector performance for 60 and 80 keV electrons arXiv:1608.07586
[64] McVitie S, McGrouther D, McFadzean S, MacLaren D A, O'Shea K J and Benitez M J 2015 Aberration corrected Lorentz scanning transmission electron microscopy *Ultramicroscopy* **152** 57–62
[65] Bassiri R *et al* 2014 Investigating the medium range order in amorphous Ta_2 O_5 coatings *J. Phys.: Conf. Ser.* **522** 12043
[66] Zhong-xian Z, Ru-ling M and Ping L L Z 1984 Amorphous phase formation of $Mo_{1-x}Ge_x$, $Mo_{1-x}Si_x$ films and their superconducting properties *Chin. Phys. Lett.* **1.1** 23
[67] Khasanov R, Klamut P W, Shengelaya A, Bukowski Z, Savić I M, Baines C and Keller H 2008 Muon-spin rotation measurements of the penetration depth of the Mo_3 Sb_7 superconductor *Phys. Rev.* B **78** 14502
[68] Carrington A and Manzano F 2003 Magnetic penetration depth of MgB_2 *Physica* C **385** 205–14
[69] Li J *et al* 2016 Nano-optical single-photon response mapping of waveguide integrated molybdenum silicide (MoSi) superconducting nanowires *Opt. Express* **24** 13931
[70] Nunes C A, Coelho G C and Ramos A S 2001 On the invariant reactions in the Mo-rich portion of the Mo–Si system *J. Phase Equilib.* **22** 556–9